doi:10.1038/nature12278

1. Supplementary Figures:

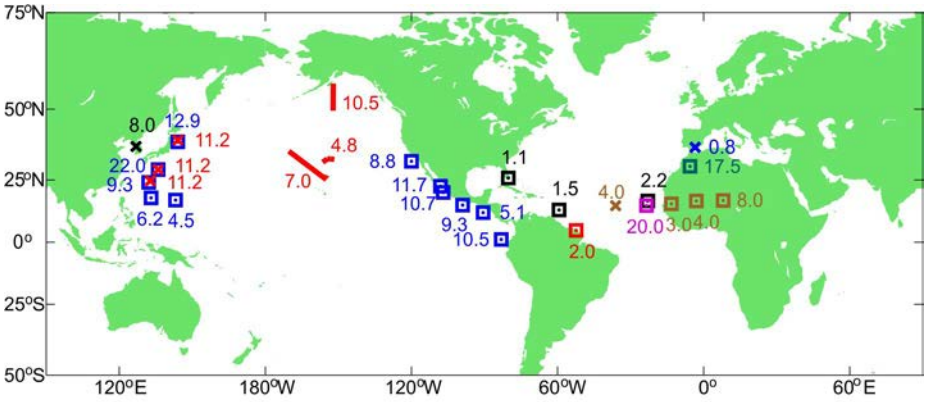

Supplementary Figure 1. **Locations of the sampling campaigns listed in Supplementary Table 1.** Numerical values refer to the total reported feldspar percentage observed at that location. Left to right: black cross: Jeong[16]; blue squares: Leinen *et al.*[31] (only provided Na/Ca-feldspar and did not report K-feldspar); red crosses: Blank *et al.*[32] (only provided Na/Ca-feldspar fraction averaged over all sites); red lines: Arnold *et al.*[33] (only Na/Ca-feldspar measured); black squares: Glaccum and Prospero[13]; red square: Prospero *et al.*[34]; brown (squares: land stations; cross: approximate location of ship-borne observation): Schütz and Sebert[35]; purple square: Kandler *et al.*[19] (2011); green square: Kandler *et al.*[36](2009); blue cross: Díaz-Hernández *et al.*[37]. Where multiple observations are represented by a single point due to space restrictions the mean of those observations is provided.

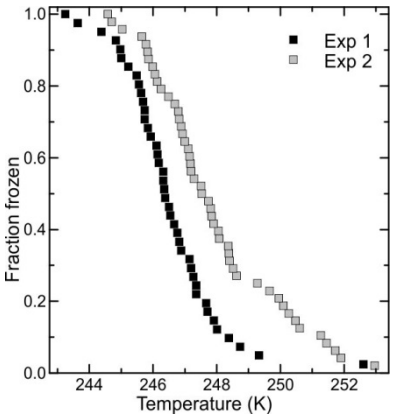

Supplementary Figure 2. Freezing of 'pure' water droplets in microlitre experiments. These experiments form the baseline for differentiating heterogeneous freezing due to an added material from freezing due to contaminants in the water and the substrate. For comparison, the coldest K-feldspar freezing event recorded by this equipment shown in Figure 3 is 257 K.

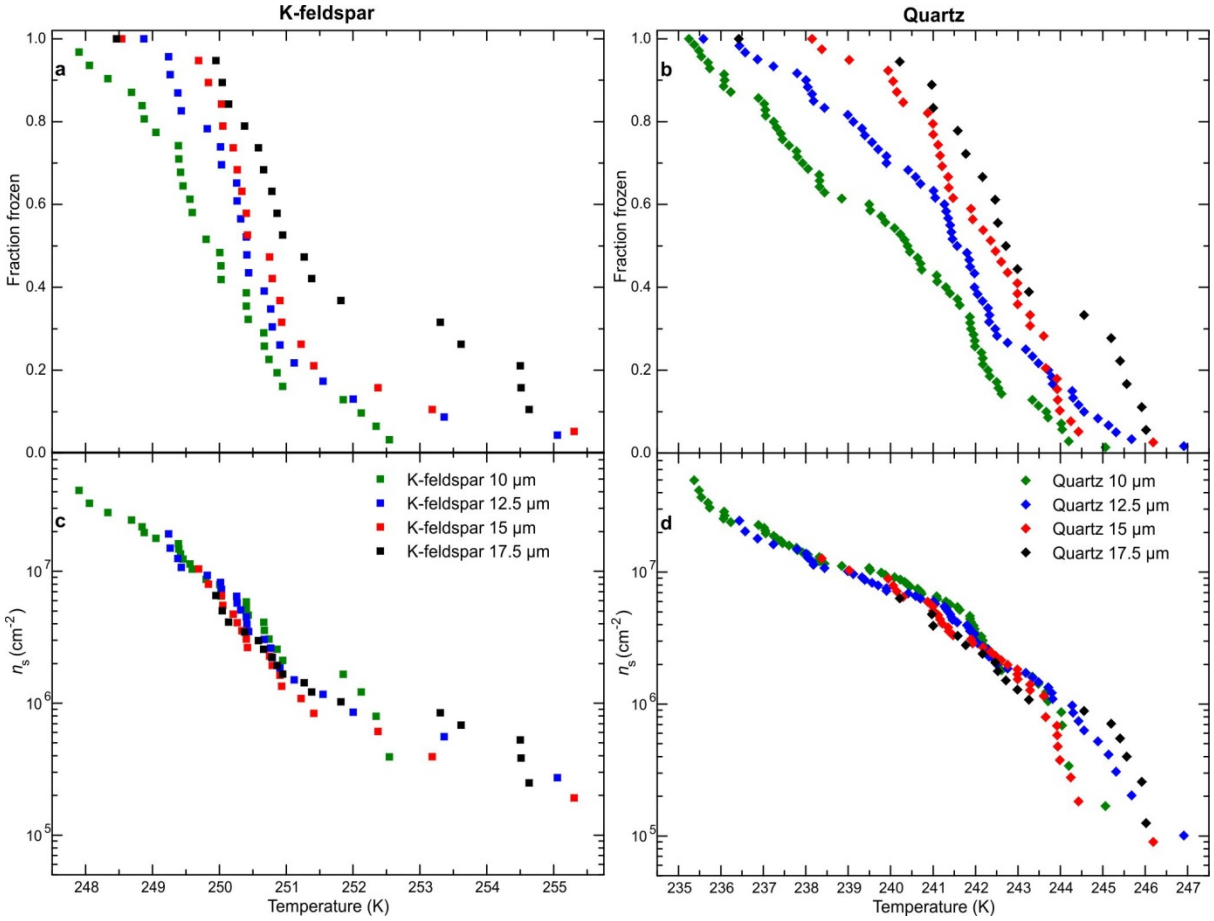

Supplementary Figure 3. Comparison of fraction frozen data and n_s values between droplet size bins for K-feldspar and quartz. Droplet sizes in diameter for each bin are shown in the figure legends. Using the BET measurements in Supplementary table 3, we estimate that the smallest droplets in the K-feldspar experiments contained ~5 average sized particles per droplet. This is discussed in the section 'Determination of ice nucleation efficiency (n_s)'.

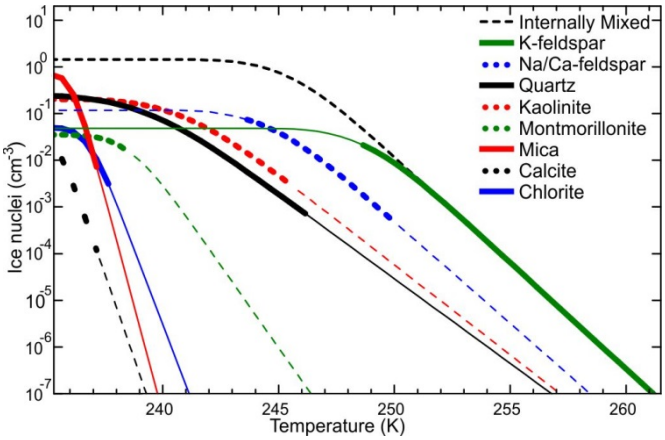

Supplementary Figure 4. Ice nuclei concentrations with enhanced clay particle surface areas. Clay particle surface areas were enhanced by a factor of 100 over that shown in Figure 2 (main paper); quartz, feldspar and calcite surface areas and overall particle concentrations remain as in Figure 2.

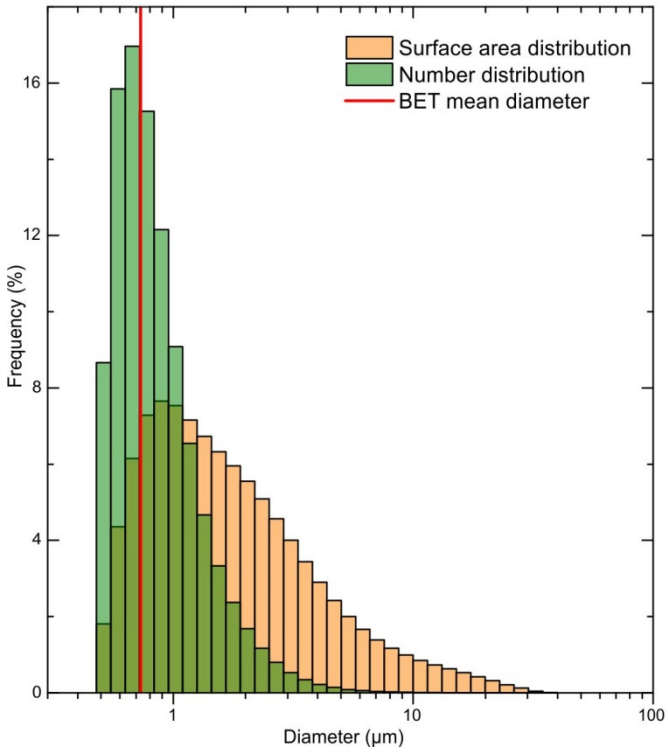

Supplementary Figure 5. Surface area and number distribution for the K-feldspar sample suspended in water. The mean surface area particle diameter from BET measurements (from Supplementary Table 3) is shown for comparison. The size distribution was measured using a Malvern Mastersizer 2000E laser diffraction instrument. The specific surface area calculated from this distribution is 0.89 m^2 g^{-1}, a factor of 3.5 smaller than that derived from the gas adsorption technique. Note that the laser diffraction technique is insensitive to the smallest particles in the distribution and this results in the distribution falling away too sharply at smaller sizes and an underestimate in specific surface area.

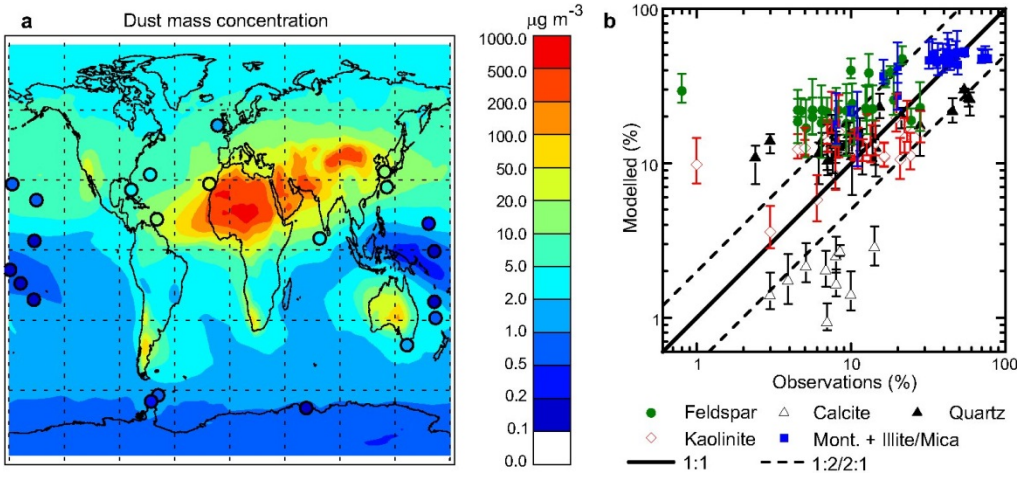

Supplementary Figure 6. Comparison of modelled mineral dust with observations. a, Modelled dust mass concentrations compared with surface measurements from Woodward *et al.*[38]. **b,** Modelled near-surface dust compositions compared with observations (Supplementary Table 1). The contribution from chlorite to the modelled surface mineralogy was not available and is not considered. The feldspar observations show the total reported feldspar proportion. In a number of the older studies only plagioclase (Na/Ca-feldspar) was reported, hence the 'total reported feldspar' may lack the K-feldspar component. This is discussed further in the Supplementary Discussion below. Vertical error bars represent the maximum and minimum modelled monthly mean values

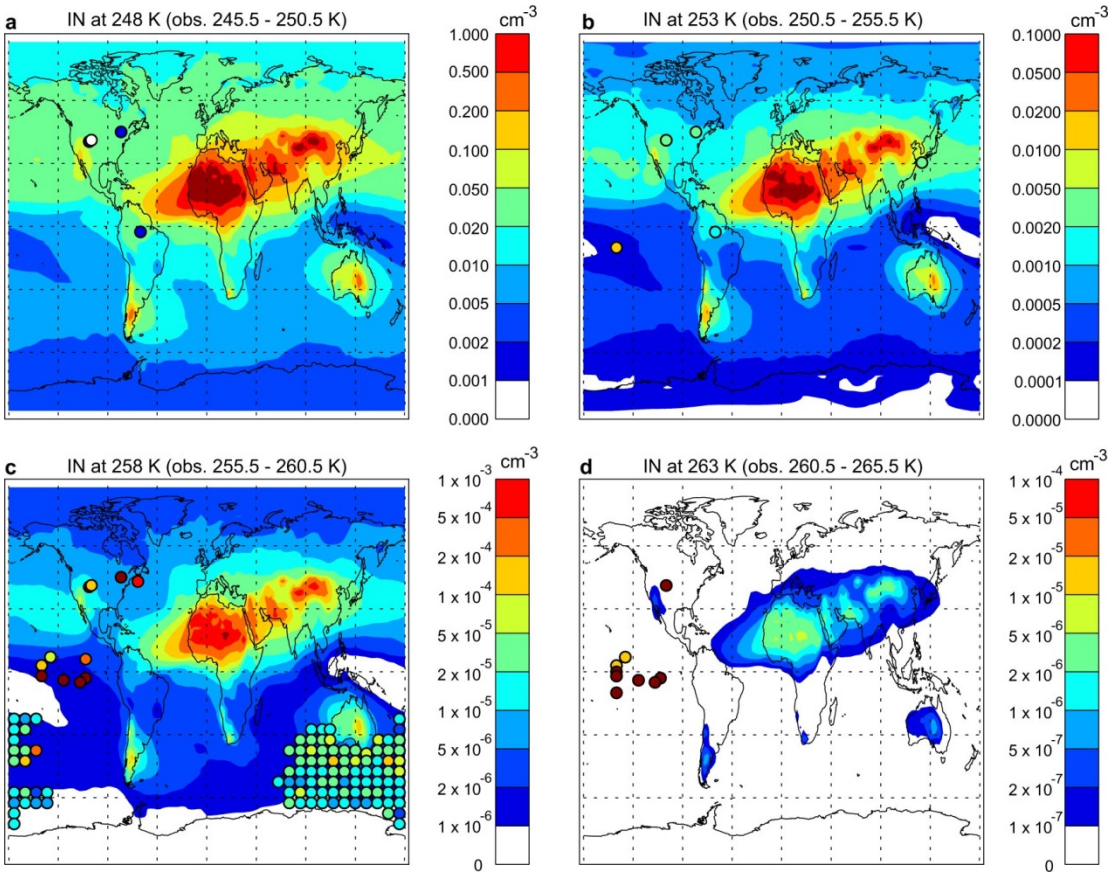

Supplementary Figure 7. Spatial comparison of model feldspar IN concentration with field data. The model IN concentrations are for four specific temperatures, whereas the field IN measurements (indicated by coloured circles, see Supplementary Table 4 and Supplementary Discussion for more details of observations) are for a range of temperatures as specified in each plot.

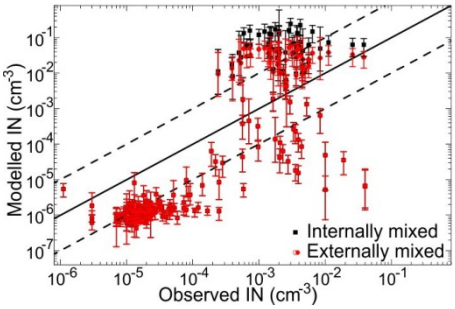

Supplementary Figure 8. Modelled versus observed K-feldspar IN concentrations, comparing different modelled mixing assumptions. Observations and annual mean modelled data ranges and sources are as in Figure 4f. In the internally mixed assumption, IN concentrations are calculated using Supplementary Equation 1 and the externally mixed assumption using Supplementary Equation 2. Vertical error bars represent the maximum and minimum modelled monthly mean values.

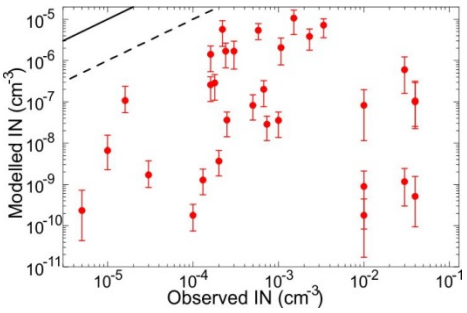

Supplementary Figure 9. Comparison of modelled K-feldspar IN concentrations with observations at temperatures above 258 K. A 1:1 line (solid) and 10:1 line (dashed) are also shown. Vertical error bars represent the maximum and minimum modelled monthly mean values.

2. Supplementary Methods

Description of experimental method

Droplet freezing assay experiments were performed using micron sized droplets in a manner similar to previously described[4,7]. A discussion of the specific materials used and differences between the literature method and the current method is provided here. In these experiments suspensions of mineral dust were created by adding a known mass of mineral to ultra-pure (18.2 MΩ cm, 0.22 μm filtered) water, which was stirred to distribute material evenly and break up aggregates.

Picolitre droplet experiments

Mineral containing droplets were deposited onto a siliconised glass slide (Hampton Research, USA, HR3-278T) using a glass nebuliser. The resulting picolitre volume droplets were then covered in silicon oil to prevent evaporation and Bergeron-Findeisen like mass transfer during freezing. Temperature measurement and logging were provided by Platinum Resistance Thermometer (PRT, Fluke 5622-05) linked to a microprocessor temperature controller (Eurotherm 2416). PRT probes were calibrated against a standard probe (Fluke 5608) and temperatures logged using a Fluke 1524 thermometer; the temperature error is ± 0.2 K. Freezing was observed using an optical microscope at 10X magnification and recorded at five frames per second using a digital camera. The fraction frozen was plotted as a function of temperature and variability (shown in Figure 1a) in this quantity was estimated from the scatter around the best fit line. This best fit line was determined using the fitted n_s curve. We did not base the statistical variability on repeat freezing experiments, because there were differences in droplet size distributions between experiments which affect fraction frozen curves (this does not affect n_s because differences in mean droplet size were taken into account).

Microlitre droplet experiments

The microlitre experiments were similar to the picolitre experiments, with the following exceptions. Droplets of dust suspension of a 1 ± 0.2 microlitre volume were pipetted onto a 22 mm diameter siliconised glass slide (Hampton Research, USA, HR3-231) using a Sartorius Biohit Picus 0.2-10 μl electronic pipette. This slide was then placed onto the flat stage of a Grant-Asymptote EF600 Stirling cooling engine. The EF600 was used to cool the slide at a rate of 1 K min^{-1} and also to log temperature at the surface of the cold plate. We estimate a temperature uncertainty of ± 0.4 K based on dodecane, 1-octanol and undecane melting points. The experiment is shielded from the atmosphere by a Perspex chamber, sealed to the cold plate using silicon vacuum grease and to a digital camera at the top. The chamber was continuously evacuated with a flow of dry N_2 at 0.3 L

min^{-1}, preventing the growth of frost between droplets that could induce freezing in other droplets. Freezing experiments were recorded at 1 frame per second, with freezing monitored visually. Control experiments with ultra-pure water droplets of this size have also been performed (Supplementary Figure 2) and show that results from this experiment are reliable down to 253 K.

Determination of ice nucleation efficiency (n_s)

We use our experimental data to derive the ice active site surface density (n_s). This parameter has been widely used as an experiment-independent parameter describing the efficiency with which a material nucleates ice[2,11,14,15]. The process of deriving n_s from experimental data from our experiments has been described previously[4,7]. Here we address issues which are pertinent to this paper.

In this analysis we need to know the surface area of dust per droplet. We use a gas adsorption technique to quantify specific surface area (surface area per unit mass of dust) of the dry powder and we can then determine the surface area per droplet using the mass of dust per droplet. A method of determining specific surface area in an aerosol sample is to use a light scattering or a particle mobility technique to establish the size distribution and assume the particles are compact spheres[1,10,11]. It has been noted for clay samples, where the individual grains are only 10s of nanometres, that the BET surface area is orders of magnitude larger than the surface area based on compact spheres[1,2,7]. Broadley *et al.*[7] present an electron microscope image of a typical micron sized clay-rich particle which is clearly an aggregate of many smaller grains and consequently has a much higher surface area than an equivalent compact sphere. For a material such as feldspar, where the primary grain sizes tend to be much larger than for clays, the discrepancies between gas adsorption measurements and those based on size distributions are much less significant.

We have examined the size distribution of particles in K-feldspar suspensions using a Malvern Mastersizer 2000E laser diffraction instrument and the resulting distribution is plotted in Supplementary Figure 5. The specific surface area determined on the basis of this distribution is 3.5 times smaller than that determined by BET. It should be noted that the laser diffraction technique is insensitive to the smallest particles in the distribution and may therefore under-predict the specific surface area. Unlike clay rich samples, we do not expect surface areas determined for K-feldspar using gas adsorption and these other techniques to differ by more than this factor of 3.5. To put this in context, this uncertainty is equivalent to the change in n_s with a ~2 K change in temperature. While relatively minor, this uncertainty should be borne in mind when comparing our data to future datasets for ice nucleation by feldspar.

In order to determine n_s values, we make the assumption that all droplets of the same size contain the same surface area of dust. A potential problem with this approach is that smaller droplets may not contain a representative number of dust particles and indeed some droplets may contain no solid particles. In order to show that the assumption that each droplet contains a representative amount of dust is valid, we show data for multiple droplet sizes in Supplementary Figure 3. This figure shows the fraction frozen curves for four size bins for two separate experiments. As expected, the freezing temperatures for the smallest droplets (which contain less particles) are lower than the larger droplets. On average each 10 μm droplet in the K-feldspar experiment contains five particles and the droplets in the largest size bin each contain 27 particles. When this data is used to derive n_s values (i.e. normalised to surface area per droplet), the agreement between the size bins is good, supporting our assumption that each droplet contains a representative surface area.

Detailed description of GLOMAP modelling procedure

GLOMAP is a size- and composition-resolving two-moment microphysical aerosol scheme, originally developed with a sectional (bin) representation of the aerosol size distribution. GLOMAP has subsequently been adapted to run with a more computationally efficient modal representation of the aerosol distribution (GLOMAP-mode[39]). The sectional version, GLOMAP-bin, is used here for its more detailed representation of size and number. GLOMAP-bin is run within the TOMCAT chemical transport model[28], and driven by ERA-40 reanalysis meteorology[40]. Meteorology for the year 2000 is used here. Horizontal resolution is 2.8°, and there are 31 vertical levels between the surface and 10 hPa. GLOMAP-bin has previously been used to simulate atmospheric mineral dust by Manktelow *et al.*[41], and Shi *et al.*[29].

GLOMAP is usually run with several advected aerosol components, typically sulfate (and associated chemistry), sea-salt, black carbon, organic carbon, and dust. In order to limit the computational cost of the simulations in the present study, only dust is retained. Dust emission fluxes and sizes are prescribed from Dentener *et al.*[30]. Eight extra advected components are added to represent the different minerals commonly observed within mineral dust as specified in Nickovic *et al.*[18] (quartz, feldspars, calcite, illite, montmorillonite (a key member of the smectite group), kaolinite, haematite, and gypsum). At some locations in the Nickovic *et al.*[18] dataset, the eight listed mineral types do not account for the full 100% of the mineral content; hence an additional unknown mineral component has been added to account for this. This unspecified mineral was always a minor contribution to the total dust. For the present simulations, dust is represented in 12 size bins, ranging from 0.1 μm to >20.0 μm diameter. The relevant mineral fraction is applied to each size bin

at the point of dust emission. GLOMAP tracks the mass mixing ratio of each mineral component and the number of particles within each size bin. Minerals are assumed to be internally mixed within each size bin.

The soil mineralogy dataset[18] used here is an update to the Claquin *et al*. dataset[42] and divides the mineral fractions into two size fractions: clay and silt. The soil mineralogy dataset was mapped onto the GLOMAP-bin size distribution by applying the mineralogy of clay-size fractions to dust particles emitted at sizes less than 2.0 μm dry diameter and silt-size at greater than 2.0 μm. Feldspar was not included in the clay size fraction of the soil mineralogical dataset, despite being observed in clay sized particles in the atmosphere[36]. To account for feldspars in the clay sized fraction in the model, it was assumed that the same feldspar to quartz ratio exists within both the clay and silt sized fraction. Different feldspar types are not resolved in Nickovic *et al*.[18]; K-feldspar is assumed to account for 35% of total feldspar based upon observations used in Supplementary Table 1 which specified both K-feldspar and Na/Ca-feldspar concentrations.

Daily varying dust emissions are prescribed from AEROCOM recommendations[30], and are relevant to the year 2000. In the present model simulations, dust is removed by wet (including impact scavenging) and dry deposition. The dust is assumed to be non-hygroscopic at emission and nucleation scavenging (by rain and ice) is not allowed. In the standard GLOMAP configuration, dust is 'aged' after condensation of sulphuric acid, and coagulation with other hygroscopic components. This ageing process is neglected here, due to the lack of other aerosol components. Sedimentation and dry deposition is calculated following Zhang *et al*. [43], and is applied for each of the 12 different particle size bins.

GLOMAP's ability to resolve global dust mass concentrations is evaluated by comparison to in situ measurements detailed in Woodward *et al*.[38] (Supplementary Figure 6a). The model does a good job of predicting dust mass concentrations in the Saharan outflow, but over predicts dust mass concentration at remote marine locations. This over prediction is consistent with the lack of removal by nucleation scavenging.

Calculation of IN concentrations

The method to calculate IN concentrations is based upon a time-independent method described previously[2,4,11,14,15], using two assumptions about aerosol mixing state. Under the internal mixing assumption, the time-independent equation is rearranged and the particle surface area modified by

the K-feldspar fraction to calculate the temperature-dependent IN concentration from each particle size bin:

$$IN_i(T) = n_i\,(1 - e\,[-\,n_s(T)\,\sigma_i\,(V_{kf} / V_i)\,]\,) \qquad \text{Supplementary Equation 1}$$

Where n_s is the time-independent nucleation site density (cm^{-2}), n_i is the concentration of particles of surface area σ_i, in size bin i. V_i and V_{kf} are the volumes of the whole dust population and the K-feldspar fraction respectively. Using the modelled total dust and K-feldspar concentrations, the total ice nuclei concentration, calculated individually for each size bin ($IN_i(T)$), can be summed for a given temperature.

Under the external mixing assumption, rather than modifying the particle surface area, the K-feldspar fraction directly modifies the number of particles:

$$IN_i(T) = n_i\,(V_{kf} / V_i)\,(1 - e\,[-\,n_s(T)\,\sigma_i\,]\,) \qquad \text{Supplementary Equation 2}$$

When the fraction of aerosol activated to ice is less than 10%, the two assumptions produce approximately the same $IN_i(T)$. This can be seen graphically in Figure 2, and explains why, in Supplementary Figure 8, the externally and internally mixed assumptions have the same result at lower IN concentrations but differ at higher concentrations.

3. Supplementary Tables

Reference	Location	IL/MI	KA	MO	CH	QU	KF	NCF	CA	OT	Trans.
Glaccum[13]	Cape Verde	53.7	6.6	0.0	4.3	19.6	2.2	5.4	8.2	0.0	Y
Glaccum[13]	Barbados	64.3	8.3	0.0	4.1	13.8	1.5	4.1	3.9	0.0	Y
Glaccum[13]	Miami	62.3	7.1	0.0	3.9	14.2	1.1	4.5	6.9	0.0	Y
Prospero[34]	French Guiana	62.0	10.0	0.0	5.0	8.0	2.0	5.0	1.0	7.0	Y
Prospero[34]	French Guiana	26.0	5.0	0.0	4.0	21.0	1.0	8.0	5.0	30.0	N
Blank[32]*	NW. Pacific	39.5	15.5	1.1	2.7	10.5	-*	11.2	-*	19.5	Y
Schutz[35]	Niger	2.0	6.0	8.0	1.0	54.0	8.0	10.0	8.0	3.0	N
Schutz[35]	Mali	4.0	7.0	7.0	3.0	59.0	4.0	6.0	7.0	3.0	N
Schutz[35]	Senegal	6.0	5.0	2.0	4.0	58.0	3.0	10.0	10.0	2.0	N
Schutz[35]	N. Atlantic	4.0	6.0	6.0	2.0	57.0	4.0	8.0	6.0	7.0	Y
Leinen[31]*	E. Pacific	37.2	17.6	5.4	2.3	7.3	-*	10.7	-*	19.5	Y
Leinen[31]*	W. Pacific	38.6	15.0	0.9	2.6	9.4	-*	13.8	-*	19.7	Y
Arnold[33]*	NW. Pacific	68.7	9.1	3.0	5.0	7.1	-*	7.1	-*	0.0	Y
Jeong[16]	South Korea	19.0	1.0	1.0	2.0	28.0	8.0	11.0	8.0	22.0	N
Kandler[36]	Morrocco (storm)	11.0	2.0	0.0	2.0	67.0	10.0	4.0	3.0	1.0	N
Kandler[36]	Morrocco	26.0	4.0	0.0	3.0	24.0	25.0	4.0	14.0	0.0	N
Kandler[19]	Cape Verde	14.0	35.0	6.0	0.0	11.0	20.0	6.0	2.0	6.0	Y
Díaz-Hernández[37]†	Spain	7.1	7.9	9.1	3.6	21.3	-†	0.8†	14.2	36.0	N
All observations mean		30.3	9.3	2.8	3.0	27.2	5.0	7.2	5.4	9.8	
All observations st.dev.		23.7	7.8	3.2	1.3	21.2	7.1	3.4	4.6	11.6	
Transported observations mean		44.4	13.0	2.2	3.2	15.8	3.1	7.6	2.8	7.9	
Transported observations st.dev		22.0	8.7	2.6	1.6	15.0	6.1	3.3	3.2	8.6	

Supplementary Table 1. **Summary of aerosol mineralogy observations,** in weight percent. IL – illite, MI – Mica, KA – kaolinite, MO – montmorillonite, CH – chlorite, QU – quartz, KF – K-feldspar (microcline), NCF – Na/Ca-feldspar (plagioclase), CA – calcite, OT – other minerals includes less common minerals, such as gibbsite, goethite, gypsum, haematite, halite, palygorskite and unidentified material. Column 'Trans.' shows which observations which have been identified as transported a large distance from source (100s to 1000s of km).*: These authors only tested for the six mineral types provided and did not report the K-feldspar or calcite fractions. †: This author only reported for total feldspar.

Mineral / Sample	IL/MI	KA	MM	CH	QU	NCF	KF	CA	Others
Mica	98.2	ND	ND	ND	ND	ND	ND	ND	Unidentified 1.8
Montmorillonite	ND	ND	67	ND	3	ND	ND	ND	Opal-CT 30.0
Chlorite	ND	ND	ND	99.6	ND	ND	ND	ND	Unidentified 0.4
Quartz	ND	ND	ND	ND	98.6	ND	ND	ND	Unidentified 1.4
Na/Ca-feldspar	ND	ND	ND	ND	4.0	76.6	16.7	ND	Ilmenite 1.8, unidentified 0.9
K-feldspar	ND	ND	ND	ND	3.9	16.0	80.1	ND	ND
Calcite	ND	ND	ND	ND	ND	ND	ND	99.6	Unidentified 0.4
K-SA	5.4	82.7	*	ND	5.9	0.4	4.5	0.3	Dolomite 0.5, unidentified 0.2
M KSF	10.3	3.3	57.0*	ND	4.3	1.6	1.7	0.9	Illite-smectite 18.3, barite 1.3, anatase 1.2
M K-10	17.6	ND	40.1*	ND	10.5	6.5	3.2	ND	Illite-smectite 20.6, zincite 0.9, halite 0.5
M SWy-2†	<1	<1	75	<1	8	16 (combined)†		ND	Gypsum 1.0
KA	ND	96	ND	ND	ND	ND	ND	ND	Anatase 3, crandallite 1
ATD	7.5	2.0	*	ND	17.1	12.4	20.3	4.3	Illite-smectite 10.1, dolomite 1.3, hematite 0.7, unidentified 25.0
NX Illite	60.5	7.2	ND	ND	6.6	1.7	8.1	2.1	Illite-smectite 13.8

Supplementary Table 2. Mineralogy of experimental samples and of dusts commonly used in the literature. Proportion of each mineral is expressed in weight percent. Mineral abbreviations as per Supplementary Table 1. Examples of commercially available minerals have been analysed by X-ray Diffraction (XRD, see for example Broadley *et al.*[7] for methodology); these were: K-SA, a kaolinite provided by Fluka/Sigma Aldrich used by Lüönd *et al.*[5] and Pinti *et al.*[6]; M KSF, a montmorillonite from Sigma Aldrich used by Pinti *et al.*[6]; M K-10, a montmorillonite from Alfa Aesar used by Pinti *et al.*[6]. Composition of other mineral dusts used in the literature is shown for comparison – KGa-1b from Murray *et al.*[4], ATD and NX illite from Murray *et al.*[2]. Further details for experimental samples used in this study are provided in Supplementary Table 3. ND – not detected. *: Montmorillonite was not directly detected; in M KSF and M K-10 the montmorillonite contribution is calculated by normalisation to 100% versus an added standard; in K-SA and ATD if any montmorillonite is present its contribution will form part of the unidentified mass. †: M SWy-2 is a montmorillonite supplied by the Clay Mineral Society, with compositional data provided by Chipera and Bish[44], who provided a total feldspar contribution of 16% rather than K-feldspar and Na/Ca-feldspar separately. Illite-smectite is a clay made of mixed layers of illite and smectite/montmorillonite. Catalogue/batch numbers for the commercial dusts sampled are: K-SA cat. no. 03584, batch no. 1143864 51906023; M KSF cat. no. 281530, batch no. S44555V; M K-10 cat. no. L15160, batch no. E06T007.

Mineral	Source	SSA ($m^2 g^{-1}$)	BET dia. (μm)	X (%)	Purity (%)
Calcite	In house	6.0	0.4	2.8	99.6
Chlorite	In house	25.0	0.08	3.2	99.6
K-feldspar	Bureau of Analysed Samples, UK	3.2	0.7	3.1	80.4
Na/Ca-feldspar	Bureau of Analysed Samples, UK	5.8	0.4	7.6	76.6
Mica	SJ Mica, USA	28.2	0.08	44.4	98.2
Montmorillonite	Clay Min. Soc., USA	91.4	0.03	2.2	67.0*
Quartz	Riedel-De Haën (Sigma Aldrich)	2.7	0.8	15.8	98.6

Supplementary Table 3. Additional characteristics of experimental mineral samples. Mineral abbreviations as per Supplementary Table 1. Na/Ca feldspar is an example of albite, a plagioclase feldspar, and is the chemical standard BCS 375; K-feldspar is the standard BCS 376; Montmorillonite is sample STx-1 from the Clay Mineral Society. The montmorillonite was used as supplied whereas all other minerals were supplied as coarse powders or pebbles and required grinding to generate fine dust particles. Grinding was performed dry with either an agate mortar and pestle (3 inch diameter mortar and ¾ inch diameter pestle) or an agate ball mill (a cylindrical vessel 2¼ inch diameter and 2¾ inch high, with two ½ inch balls). XRD analysis (Supplementary Table 2) was performed after grinding, during which no agate was detected. SSA: specific surface area of the sample measured after any grinding took place, utilising the BET N_2 adsorption method using a Micromeritics TriStar 3000. BET dia.: the surface area mean particle diameter calculated using the surface area to mass ratio supplied by the SSA measurement assuming particles are spherical (diameter = 2 × 3/(SSA × density)). x: the contribution of this mineral to the mean observations as per Supplementary Table 1 (kaolinite: 13.0%, others 7.9%). *: Value taken from Chipera and Bish[44].

Campaign	Location	Latitude	Longitude	Altitude	Temperature (K)	No. obs.	Measurement technique
Amaze-08[45]	Brazil	-2.595	-60.209	Surface	241 – 255	63	CFDC
Bigg 73[46]	South of Australia	-20 – -75	-70 – 140	Surface	258	102	Filter
Clex[45]	East Canada	45	-78	450 – 920 hPa	238 – 259	60	CFDC
Ice-L[45]	Central USA	41.1	-104.8	385 – 724 hPa	238 – 252	32	CFDC
Inspect I[45]	Central USA	40.455	-106.744	Surface	239 – 246	13	CFDC
Inspect II[45]	Central USA	40.455	-106.744	Surface	241 – 258	11	CFDC
Rosinski 87[47]	Central Pacific	7 – -10	-110 – 150	Surface	254 – 270	33	Filter
Rosinski 95[48]	East China Sea	30.5	127.5	Surface	253	1	Filter
Schnell 77[49]	Eastern Canada	43	-62.5	Surface	258	2	Filter
Wisp 94[45]	Central USA	41.1	-104.8	340 – 880 hPa	254 – 264	20	CFDC

Supplementary Table 4. Summary of ice nuclei observational campaigns. Temperatures reported refer to the temperature of the analysis for IN (processing temperature) rather than ambient temperature at the sampling location. Only measurements taken at or above water saturation are shown.

4. Supplementary Discussion

Comparison between modelled and observed dust mineralogy, concentration and derived IN concentrations.

Dust concentration. The annual mean surface concentration of mineral dust is compared with observations in Supplementary Figure 6a. Overall, the model predicts dust concentrations well, with the possible exception of locations far from source where the model tends to over-predict dust concentrations (such as the middle of the Pacific and high latitudes). The lack of nucleation scavenging in the model may lead to dust concentrations which are too large.

Dust mineralogy.

To test the quality of the mineralogy of global mineral dusts, the modelled dust compositions are compared with observations. The mineralogy observations, from a number of authors, are all made at or near the surface. The standard methodology of determining dust mineralogy is to expose a

filter/mesh to the atmosphere for a number of hours/days and then to use XRD in a laboratory to quantify mineralogy (see for example Kandler *et al.*[36]). A number of older observations[31-33] used XRD techniques were limited in the minerals that could be retrieved and did not report K-feldspar and Calcite fractions. Observations, especially in the higher latitudes and Asia, are sparse. See Supplementary Figure 1 and Supplementary Table 1 for details of observations. In Supplementary Figure 1 and Supplementary Figure 6b we report the 'total observed feldspar'. In some of the older studies only the Na/Ca-feldspar component was estimated and the K-feldspar component was not provided, which may imply the total reported feldspar was smaller than the actual total feldspar component in those samples (see Supplementary Table 1 for details).

A comparison of the annually averaged mineralogy from the model with the observations is shown in Supplementary Figure 6b. The soil mineralogy map[18], and hence model, only contains total feldspar rather than K and Na/Ca-feldspar separately. In general, the model reproduces the observed mineralogy well. The model tends to over-predict the feldspar content of dust, especially for lower mass fractions. This is possibly due to the lack of nucleation scavenging within the model; since feldspars are efficient IN they may be removed from the atmosphere faster than the other mineral types. Also, we neglect chemical processing which may also preferentially remove feldspar. In addition, the observed feldspar is the total reported feldspar and in some observations the feldspar component may be underestimated. It is important to note that the over-prediction of the feldspar proportion by a factor of two does not alter the conclusion that feldspar dominates ice nucleation by mineral dust and introduces an uncertainty in IN concentrations much smaller than the natural variability.

IN concentrations. The modelled IN concentrations are compared to the observed values in Figure 4f and also in Supplementary Figures 6, 7 and 8. We only compare to observations where particles were tested for ice nucleation at or above water saturation where the likely mode of nucleation was condensation/immersion and therefore comparable with our measurements. We also only compare to observations where collection location, pressure and processing temperature were reported.

The observations were made using either a Continuous Flow Diffusion Chamber (CFDC) or filter technique. The CFDC technique involves exposing aerosol particles to a specific temperature and supersaturation and counting the number of ice crystals which form (see DeMott *et al.*[45] and references therein). The filter based technique involves drawing a known volume of air through a filter and detecting ice nuclei on that filter using a diffusion chamber or droplet freezing methodology[49].

In Supplementary Figure 7, we have plotted the IN concentrations according to their geographic location and grouped the observations into four temperature bins. One thing to note is that there are very few measurements around the globe and what exists is limited to narrow ranges of processing temperature (also see Supplementary Table 4). When making this comparison it should also be borne in mind that the measurements tend to be for discrete points in space and time, whereas the model output is an annual average from a large gridbox. The variability in the monthly averages is indicated in the plots. As the model does not take into account nucleation scavenging or chemical processing in the atmosphere, we suggest that agreement of about a factor of 10 between observations and annual mean model results is good.

In the main paper we discussed the comparison between model and observations on the basis of Figure 4f, which suggests that feldspar is an important aerosol component for ice nucleation below ~258 K. Inspection of Supplementary Figure 7 helps us to resolve in which regions the model is able to better reproduce the observed concentrations. The observations at 253 K and below over land are mostly within a factor of 10 of the model predictions, which indicates that feldspar is a major IN type in this temperature range in these regions. In contrast, the model greatly under-predicts the IN concentrations in the equatorial Pacific and at temperatures warmer than 258 K in general (see Supplementary Figure 9). This indicates that at warmer temperatures and in some locations, feldspar cannot account for IN concentrations and there must be a different source of IN, such as biological particles.

An analysis of the modelled IN concentrations using two different aerosol mixing state assumptions is shown in Supplementary Figure 8. The different modelled concentrations are calculated using Supplementary Equation 1 (internally mixed) and Supplementary Equation 2 (externally mixed). At temperatures above ~252 K the predicted IN concentrations are independent of mixing state, but at lower temperatures the internal assumption means that more dust aerosol contains feldspar and can therefore nucleate ice. The external assumption provides a better fit to the observations, but the mixing state of atmospheric aerosol is most likely somewhere in between these two limiting cases.

References

31 Leinen, M., Prospero, J. M., Arnold, E. & Blank, M. Mineralogy of aeolian dust reaching the north Pacific-Ocean. 1. Sampling and analysis. *J. Geophys. Res.* **99**, 21017-21023, doi:10.1029/94jd01735 (1994).

32 Blank, M., Leinen, M. & Prospero, J. M. Major Asian aeolian inputs indicated by the mineralogy of aerosols and sediments in the western North Pacific. *Nature* **314**, 84-86, doi:10.1038/314084a0 (1985).

33 Arnold, E., Merrill, J., Leinen, M. & King, J. The effect of source area and atmospheric transport on mineral aerosol collected over the North Pacific Ocean. *Global Planet. Change* **18**, 137-159, doi:10.1016/S0921-8181(98)00013-7 (1998).

34 Prospero, J. M., Glaccum, R. A. & Nees, R. T. Atmospheric transport of soil dust from Africa to South-America. *Nature* **289**, 570-572, doi:10.1038/289570a0 (1981).

35 Schütz, L. & Sebert, M. Mineral aerosols and source identification. *J. Aerosol Sci.* **18**, 1-&, doi:10.1016/0021-8502(87)90002-4 (1987).

36 Kandler, K. *et al.* Size distribution, mass concentration, chemical and mineralogical composition and derived optical parameters of the boundary layer aerosol at Tinfou, Morocco, during SAMUM 2006. *Tellus* **61B**, 32-50, doi:10.1111/j.1600-0889.2008.00385.x (2009).

37 Díaz-Hernández, J. L., Martín-Ramos, J. D. & López-Galindo, A. Quantitative analysis of mineral phases in atmospheric dust deposited in the south-eastern Iberian Peninsula. *Atmos. Environ.* **45**, 3015-3024, doi:10.1016/j.atmosenv.2011.03.024 (2011).

38 Woodward, S. Modeling the atmospheric life cycle and radiative impact of mineral dust in the Hadley Centre climate model. *J. Geophys. Res.* **106**, 18155-18166, doi:10.1029/2000jd900795 (2001).

39 Mann, G. W. *et al.* Description and evaluation of GLOMAP-mode: a modal global aerosol microphysics model for the UKCA composition-climate model. *Geosci. Model Dev.* **3**, 519-551, doi:10.5194/gmd-3-519-2010 (2010).

40 Uppala, S. M. *et al.* The ERA-40 re-analysis. *Q. J. R. Meteorol. Soc.* **131**, 2961-3012, doi:10.1256/qj.04.176 (2005).

41 Manktelow, P. T., Carslaw, K. S., Mann, G. W. & Spracklen, D. V. The impact of dust on sulfate aerosol, CN and CCN during an East Asian dust storm. *Atmos. Chem. Phys.* **10**, 365-382, doi:10.5194/acp-10-365-2010 (2010).

42 Claquin, T., Schulz, M. & Balkanski, Y. J. Modeling the mineralogy of atmospheric dust sources. *J. Geophys. Res.* **104**, 22243-22256, doi:10.1029/1999jd900416 (1999).

43 Zhang, L., Gong, S., Padro, J. & Barrie, L. A size-segregated particle dry deposition scheme for an atmospheric aerosol module. *Atmos. Environ.* **35**, 549-560, doi:10.1016/S1352-2310(00)00326-5 (2001).

44 Chipera, S. J. & Bish, D. L. Baseline studies of The Clay Minerals Society Source Clays: Powder X-ray diffraction analyses. *Clays Clay Miner.* **49**, 398-409, doi:10.1346/ccmn.2001.0490507 (2001).

45 DeMott, P. J. *et al.* Predicting global atmospheric ice nuclei distributions and their impacts on climate. *Proc. Natl. Acad. Sci. USA* **107**, 11217-11222, doi:10.1073/pnas.0910818107 (2010).

46 Bigg, E. K. Ice Nucleus Concentrations in Remote Areas. *J. Atmos. Sci.* **30**, 1153-1157, doi:10.1175/1520-0469(1973)030<1153:incira>2.0.co;2 (1973).

47 Rosinski, J., Haagenson, P. L., Nagamoto, C. T. & Parungo, F. Nature of ice-forming nuclei in marine air masses. *J. Aerosol Sci.* **18**, 291-309, doi:10.1016/0021-8502(87)90024-3 (1987).

48 Rosinski, J., Nagamoto, C. T. & Zhou, M. Y. Ice-forming nuclei over the East China Sea. *Atmos. Res.* **36**, 95-105, doi:10.1016/0169-8095(94)00029-D (1995).

49 Schnell, R. C. Ice Nuclei in Seawater, Fog Water and Marine Air off the Coast of Nova Scotia: Summer 1975. *J. Atmos. Sci.* **34**, 1299-1305, doi:10.1175/1520-0469(1977)034<1299:inisfw>2.0.co;2 (1977).